



저작자표시-비영리-변경금지 2.0 대한민국

이용자는 아래의 조건을 따르는 경우에 한하여 자유롭게

- 이 저작물을 복제, 배포, 전송, 전시, 공연 및 방송할 수 있습니다.

다음과 같은 조건을 따라야 합니다:



저작자표시. 귀하는 원저작자를 표시하여야 합니다.



비영리. 귀하는 이 저작물을 영리 목적으로 이용할 수 없습니다.



변경금지. 귀하는 이 저작물을 개작, 변형 또는 가공할 수 없습니다.

- 귀하는, 이 저작물의 재이용이나 배포의 경우, 이 저작물에 적용된 이용허락조건을 명확하게 나타내어야 합니다.
- 저작권자로부터 별도의 허가를 받으면 이러한 조건들은 적용되지 않습니다.

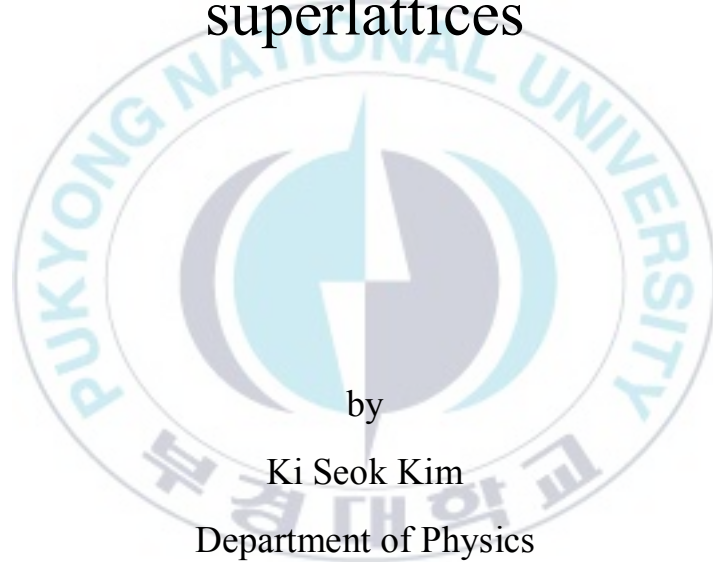
저작권법에 따른 이용자의 권리는 위의 내용에 의하여 영향을 받지 않습니다.

이것은 [이용허락규약\(Legal Code\)](#)을 이해하기 쉽게 요약한 것입니다.

[Disclaimer](#)

Thesis of the degree of Master of Physics

A study on strong correlations between
octahedral structure and physical
properties of SrRuO₃/CaRuO₃
superlattices



by

Ki Seok Kim

Department of Physics

The Graduate School

Pukyong National University

August, 2022

A study on strong correlations between
octahedral structure and physical
properties of SrRuO₃/CaRuO₃
superlattices

(SrRuO₃/CaRuO₃ 초격자 팔면체 구조와
물성 간의 강한 상관관계에 관한 연구)

Advisor: Prof. Jae-Yeol Hwang

by

Ki Seok Kim

A thesis submitted in partial fulfillment of the requirements
for the degree of Master of Physics

Department of Physics, The Graduate School,

Pukyong National University

August, 2022

A study on strong correlations between octahedral structure and
physical properties of SrRuO₃/CaRuO₃ superlattices

A dissertation

by

Ki Seok Kim

Approved by:

The logo of Pukyong National University is a circular emblem. It features a central stylized design with a blue and grey color scheme, possibly representing a compass or a similar symbol. The words "PUKYONG NATIONAL UNIVERSITY" are written in a light blue font around the perimeter of the circle.



(Chairman) Sung Heum Park



(Member) Sang A Lee



(Member) Jae-Yeol Hwang

August 26, 2022

Contents

List of Table and Figures

Abstract

1. Introduction	1
2. Theoretical background	3
2.1 Characteristic of crystal and structure.....	3
2.1.1 Strontium titanate (SrTiO_3).....	3
2.1.2 $A\text{RuO}_3$ ($A = \text{Ca}, \text{Sr}$).....	4
2.2 RuO_6 octahedral distortion.....	5
2.3 Experimental.....	6
2.3.1 Pulsed Laser Deposition (PLD).....	6
2.3.2 X-ray Diffraction (XRD).....	7
2.3.3 Ellipsometry.....	8
3. Experiment equipment and methodology	9
3.1 Thin films growth and structure characterization.....	9
3.2 Electrical measurements.....	9
3.2 Magnetic moment and resistivity measurements.....	10
4. Results & discussion	11
4.1 Structure characterizations of superlattices.....	11
4.2 Electronic and magnetic properties.....	16
4.3 Electronic structure of superlattice.....	21
4.4 Half-Order-Peak and RuO_6 octahedral distortion.....	24
4.5 Correlation between structure and magnetic property.....	31
5. Conclusion	34
Reference	36

List of Figures

Figure 1. The crystal structure of SrTiO ₃	3
Figure 2. Schematic of the RuO ₆ octahedral rotation.	4
Figure 3. The RuO ₆ octahedral rotation of ARuO ₃	5
Figure 4. Schematic figure of pulsed laser deposition (PLD) process.	6
Figure 5. Principle of Bragg's law ($n\lambda = 2d\sin\theta$).	7
Figure 6. Schematic physics of ellipsometry.	8
Figure 7. Structural characterizations of [(SrRuO ₃) ₆ /(CaRuO ₃) _m] ₁₀ superlattices grown on SrTiO ₃ (001) substrates.....	13
Figure 8. Quantitative structural analysis of [(SrRuO ₃) ₆ /(CaRuO ₃) _m] ₁₀ superlattices grown on SrTiO ₃ (001) substrates.....	14
Figure 9. X-ray diffractions of (2 0 4) reflections with φ angles of 0, 90, 180, and 270° about (SrRuO ₃) ₆ /(CaRuO ₃) _m superlattices demonstrated by [6/m]. For all the superlattices peak positions nearly located by SrTiO ₃ (204) plane reflection.	15
Figure 10. The electronic and magnetic properties of the (SrRuO ₃) ₆ /(CaRuO ₃) _m superlattices tuned by the CaRuO ₃ unit cell.	19
Figure 11. Magnetization (M) versus field (H) of (SrRuO ₃) ₆ /(CaRuO ₃) _m superlattices at $T = 5$ K for $m < 8$ unit cells (a) and $m > 6$ unit cells (b).	20
Figure 12. Spectroscopic ellipsometry spectra of the (SrRuO ₃) ₆ /(CaRuO ₃) _m superlattices.	23

Figure 13. Non-destructive identification for RuO₆ octahedral distortion of (SrRuO₃)₆/(CaRuO₃)_m superlattices by HRXRD.30

Figure 14. Correlation between RuO₆ octahedral rotation and electronic structure properties of the (SrRuO₃)₆/(CaRuO₃)_m superlattices tuned by the CaRuO₃ unit cell.33



SrRuO₃/CaRuO₃ 초격자의 팔면체 구조와 물성 간의 강한 상관관계에 관한 연구

김기석

부경대학교 대학원 물리학과

요 약

ABO₃ 페로브스카이트 산화물의 산소 팔면체 정렬구조는 이 물질군의 전자적 및 자기적 특성에 영향을 주는 중요한 원인이며, 현재 복합 산화물들의 이중 계면을 통한 팔면체 구조 변화에 대한 많은 관심이 집중되고 있다. 본 연구에서는 각 SrRuO₃ 층 및 CaRuO₃ 층에서의 팔면체 구조가 초격자 구조내에서 계면 결합을 통해 조작될 수 있으며, 이는 전자 및 자기 특성을 추가로 변화시킬 수 있음을 보여준다. SrTiO₃ 기판에서 성장한 (SrRuO₃)₆/(CaRuO₃)_{*m*} 초격자의 팔면체 회전에 대한 직접적인 관찰은 실험실 기반 고출력 X-선 회절을 이용한 비 대칭 면 분석을 통해 수행하였다. 그 결과, RuO₆ 팔면체의 회전 정도와 함께 사방정계에서 정방정계로의 SrRuO₃ 결정학적 위상의 변화가 초격자에서 SrRuO₃ 와 CaRuO₃ 사이의 이중 계면을 가로질러 연결된 팔면체의 계면 접촉에 의해 조정될 수 있음을 발견했다. 실제로 RuO₆ 팔면체 회전과 *c*-축 격자크기는 CaRuO₃ 층의 두께가 증가함에 따라 감소했다. 특히, *c*-축을 따른 다른 두 물질의 계면에서의 에피텍셜 스트레인에 의한 변형으로 인해 CaRuO₃ 층의 주기가 변화함에 따라 SrRuO₃ 의 RuO₆ 팔면체 왜곡이 체계적으로 변화하고, 그에 따른 SrRuO₃ 의 전자적 및 자기적 특성이 변조됨을 확인하였다. 마지막으로 RuO₆ 팔면체 왜곡과 물리적 특성에 영향을 미치는 전자 구조 사이의 강한 상관 관계가 밝혀졌다.

이러한 결과는 초격자 구조를 이용하여 나노 스케일에서 페로브스카이트 산화물의 팔면체 구조를 조작할 수 있으며, 다양한 페로브스카이트 물질의 물리적 특성과 팔면체 구조 간의 상관 관계를 기반으로 새로운 물성을 개발하고 응용하는데 활용될 수 있을 것으로 예상된다.

A study on strong correlations between octahedral structure and physical properties of SrRuO₃/CaRuO₃ superlattices

Ki Seok Kim

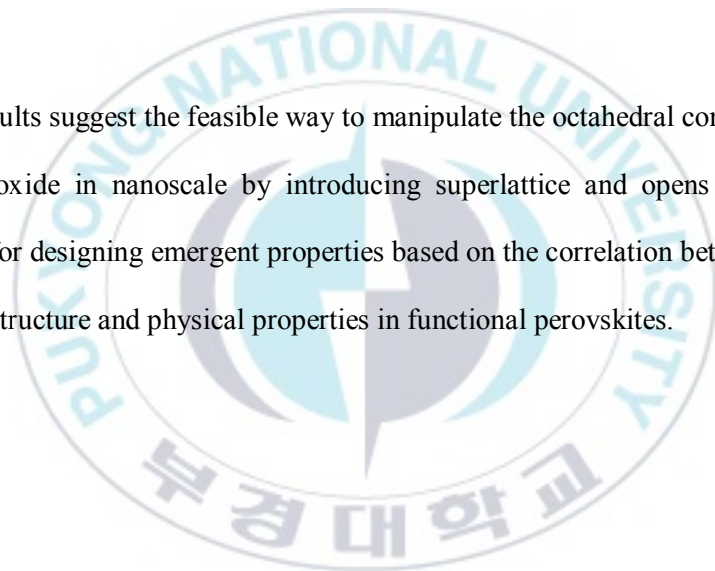
Department of Physics, The Graduate School
Pukyong National University

Abstract

Oxygen octahedral configurations attributed to lattice distortion is a key to determine the electronic and magnetic properties of the ABO_3 perovskite oxides and have been attracted a lot of interests on physics and applications of complex oxides hetero interface. In this study, we show that the octahedral structure of the SrRuO₃ layer can be manipulated by interfacial coupling with CaRuO₃ layer in superlattice, which further changes the electronic and magnetic properties. Direct observations for the octahedral rotation of (SrRuO₃)₆/(CaRuO₃)_{*m*} superlattices grown on SrTiO₃ substrates were carried out by analyzing half-order Bragg peaks using high-power X-ray diffractometer with 2D detector. We found that the change in crystallographic phase of SrRuO₃ from orthorhombic to tetragonal, accompanied by the degree of RuO₆ rotation, can be tuned by the interface coupling of the linked-octahedra across the hetero-interface between

SrRuO₃ and CaRuO₃ in superlattice. Indeed, RuO₆ octahedral rotation and *c*-axis lattice decreased with increasing the thickness of CaRuO₃ unit cell (UCs). In particular, it was also confirmed that the RuO₆ octahedral distortion of SrRuO₃ was systematically changed with altering the period of CaRuO₃ layer due to the epitaxial strain at hetero-interfaces along *c*-axis, and the electronic and magnetic characteristics of SrRuO₃ is modulated with RuO₆ octahedral distortion. Finally, a strong correlation between RuO₆ octahedral distortion and electronic structure affecting physical properties was elucidated.

These results suggest the feasible way to manipulate the octahedral configuration of perovskite oxide in nanoscale by introducing superlattice and opens a promising possibility for designing emergent properties based on the correlation between oxygen octahedral structure and physical properties in functional perovskites.



1. Introduction

Octahedral rotation in perovskite oxides ABO_3 attracted a great deal of attentions due to its critical role from strong correlations between electrons, lattices, and spins [1]. The manipulation of octahedral rotation with interface-coupling by altering artificial superlattices was possible to measure accurate octahedral rotation by X-ray diffraction (XRD). Recently, calculations with first principle have demonstrated that octahedral rotation could be modified by strain effect [2, 3], stoichiometry control[4, 5], and change of A -site cation ionic radius [6, 7]. Due to the transition metal-oxygen bonds have a large $p-d$ hybridization, the novel magnetic modulations and interactions by orbital exchange and order were changed. The ruthenium oxides family is a suitable material for observing the change of electric/magnetic properties according to octahedral distortion. Among ruthenium oxides ($ARuO_3$, $A = Ca, Sr$), $CaRuO_3$ (CRO) and $SrRuO_3$ (SRO) have been well-studied members as a part of different functional transition metal oxides (TMOs) heterostructures since it is one of the most widely used electrode materials for oxide electronics. Interestingly, CRO and SRO show the different magnetic properties by a degree of the octahedral distortion, as paramagnetic and ferromagnetic order, respectively, although they have much structural similarities[8]. Such striking difference is the subject of a long running debate[9, 10, 11, 12, 13]. These distinct different magnetic properties are described the ionic size mismatch between A - and B - (Ru) site cations, incorporating structural distortions by oxygen octahedra rotation and tilting. Intermediate strength of spin-orbit coupling of Ru, distortion of the structure according to A -site ionic increases. Theoretical

calculations have also been reported that the large octahedral distortion in CRO is responsible for the suppression of ferromagnetism compared to SRO with small distortion[14]. This indicates that the electronic and magnetic properties can be strongly dependent on octahedral distortion within the perovskite structural framework. Given the debate on the different behaviors in CRO and SRO and the many conflicting results in literature, it is interesting to study superlattices with these materials in immediate contact.

In this study, we suggest that the electronic and magnetic properties can be tailored by controlling the octahedral distortion in the artificial SRO/CRO heterostructure. To verify this concept, SRO/CRO superlattices were grown on SrTiO₃ (001) substrates by pulsed laser deposition. The structure of superlattice was controlled by altering the stacking of [(SRO)₆/(CRO)_{*m*}]₁₀ (*m* is the number of unit cell layer) and were characterized by high-resolution 6-circle X-ray diffractometer. In addition, the electronic transport and magnetic properties as a function of temperature for these superlattices were systematically analyzed with varying the periodicity of the superlattice and spectroscopic ellipsometry was also introduced to elucidate the electronic structures of the superlattices.

2. Theoretical background

2.1 Characteristic of crystal and structure

2.1.1 Strontium titanate (SrTiO_3)

Strontium titanate (SrTiO_3) is a transition metal-oxide consisting of strontium, titanium, and oxide with the chemical formula SrTiO_3 . At room temperature, SrTiO_3 crystallizes in the ABO_3 -type cubic perovskite structure (space group $Pm3m$) with a lattice parameter of 3.905 Å in bulk [15]. SrTiO_3 is an excellent substrate for epitaxial growth of many oxide-based thin films such as ruthenates ($ARuO_3$, $A = \text{Ca}, \text{Sr}, \text{Ba}$), perovskites, and others.[16, 17]. And it is useful to measure the electronic and magnetic properties of specific samples which growth on SrTiO_3 , due to SrTiO_3 is insulator with a direct bandgap of 3.75 eV [18]

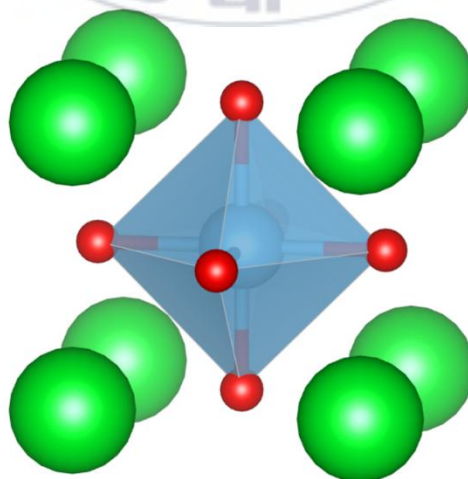


Figure 1. The crystal structure of SrTiO_3 (cubic unit cell / space group: $Pm3m$ (#221))

2.1.2 $ARuO_3$ ($A = Ca, Sr$)

The complex perovskite oxides, $ARuO_3$ ($A = Ca, Sr$), are well-known $4d$ transition metal oxides. In bulk, $SrRuO_3$ and $CaRuO_3$ have an orthorhombic structure (space group : $Pnma$ (#62)) with lattice parameters of $a_0 = 5.530$, $b_0 = 5.567$, and $c_0 = 7.845$ Å and $a_0 = 5.354$, $b_0 = 5.524$, and $c_0 = 7.649$ Å at room temperature, respectively [19]. Due to the difference of octahedral distortion. They have radically different magnetic properties. $SrRuO_3$ is a ferromagnetic metal and Fermi liquid while $CaRuO_3$ is non-magnetic metal and non-Fermi liquid [20].

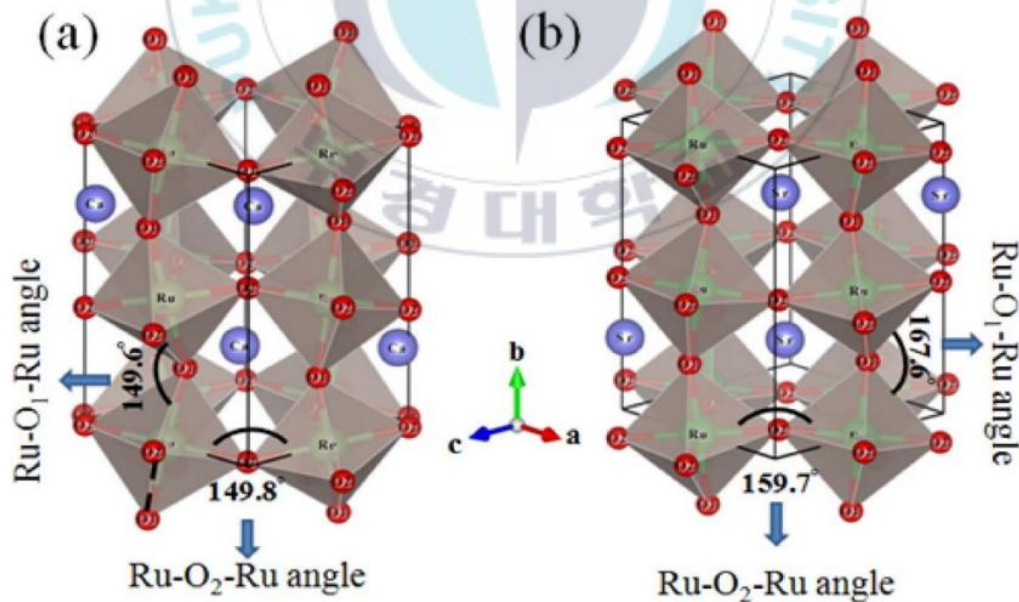


Figure 2. Schematic of the RuO_6 octahedral rotation (orthorhombic unit cell / space group: $Pnma$ (#62)) of $CaRuO_3$ (a) and $SrRuO_3$ (b) [21]

2.2 RuO₆ octahedral rotation

The octahedral rotation of the RuO₆ octahedra is consist of the Ru-O-Ru bond angles and Ru-O bond lengths. Each Ru-O-Ru bond angles and Ru-O bond lengths strongly related with hybridization of Ru transition metal with oxygen *p*-orbital and Ru *d-d* orbital coupling. Determining the modified octahedral rotations by interface-coupling in superlattices is necessary to control the electronic and magnetic properties in oxide interfaces. In particular, the strong hybridization of Ru with oxygen *p*-orbitals in ruthenates was changed by octahedral rotation, which leads the crystalline symmetries with breaking the degeneracy.[22]

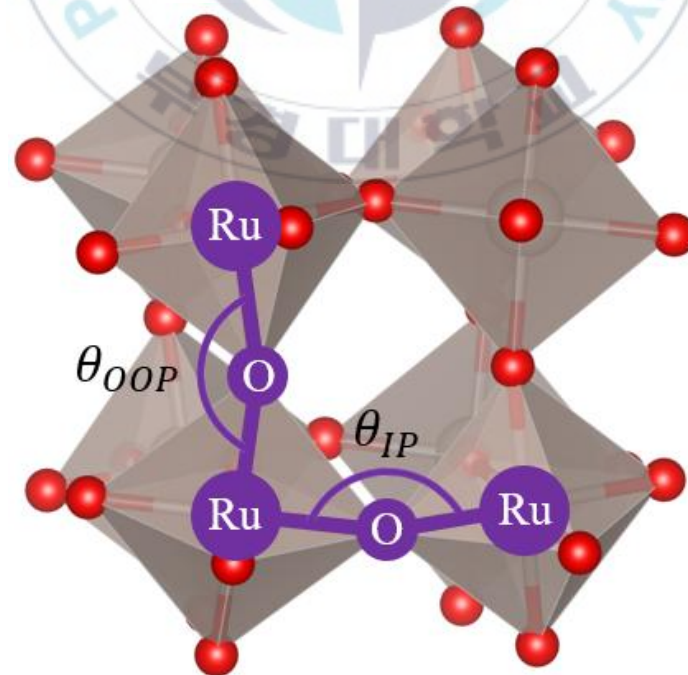


Figure 3. The RuO₆ octahedral rotation of ARuO₃

2.3 Experimental

2.3.1 Pulsed Laser Deposition (PLD)

In the thin film growth, the pulsed laser deposition (PLD) is a representative physical vapor deposition. Focused laser pulse with high energy strikes the target, inducing plume. The plume of vaporized target elements goes to substrate, and then deposited on heated substrate in controlled reduced atmosphere like oxygen. The growth of thin film depends on many processing parameters such as the pressure in chamber, background flow rate of O_2 , substrate temperature, and the repetition rate and energy of the laser beam. In accordance with each material, film growth is quite sensitive such conditions. When the pulsed laser shot is absorbed at the target, the temperature of target surface rapidly increases and lead that the ablation and evaporation of the target material. The vaporized plume expands into the vacuum chamber. The plume which consists of electrons, ions, atoms, and molecules deposits on the heated substrate.

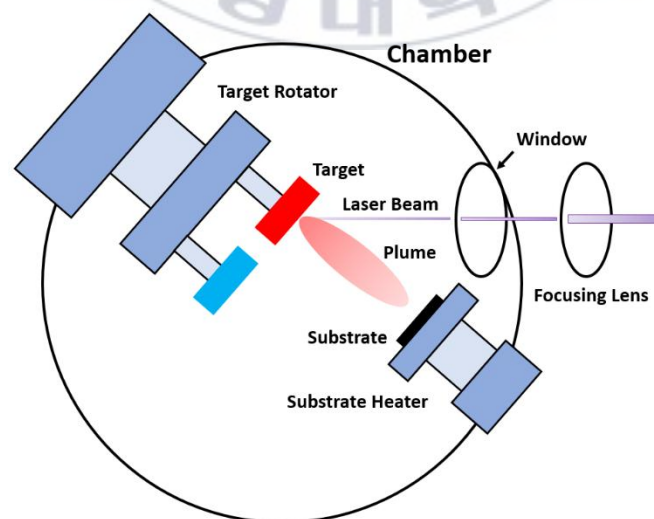


Figure 4. Schematic figure of pulsed laser deposition (PLD) process.

2.3.2 X-ray Diffraction (XRD)

X-ray diffraction (XRD) is a representative method of non-destructive analytical techniques which measure the crystal structure and symmetry. Lab scale XRD usually use the $\text{Cu-K}_{\alpha 1}$ with wavelength (λ) of 1.540562 Å. The aligned incident X-ray beams were highly diffracted specific angles, due to the periodic alignment of atoms in the crystalline material. Such phenomenon is explained by fundamental principle of XRD is based on Bragg's law, $n\lambda = 2d\sin\theta$, where n is the diffraction order ($n = 1$ is first order, and $n = 2$ is second order), λ is wavelength of X-rays, d is distance between periodic planes, and θ is the incidence angle of X-rays. In addition, The X-rays are strongly interacted with electrons in atom. Thus, intensities of diffracted X-rays depend on X-ray form factor for specific atom.

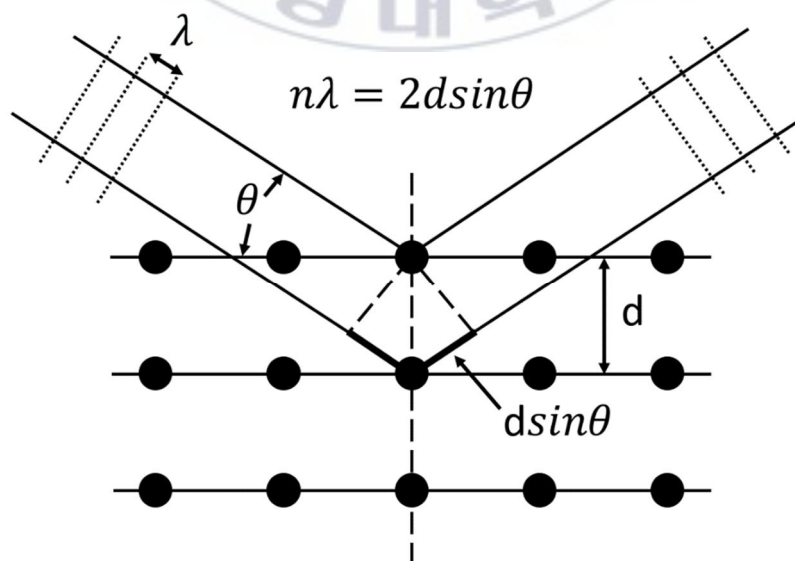


Figure 5. Principle of Bragg's law ($n\lambda = 2d\sin\theta$).

2.3.3 Ellipsometry

Ellipsometry is an optical analytical technique and method of non-destructive which measure the dielectric constant depending on wavelength of incident light, thickness, roughness, and many optical properties of thin film. Ellipsometry have less sensitive to several kinds of defects such like oxygen vacancy, long penetration depth, and k -average joint density of state. And it is an advantage to measure optical properties in comparison with such like an X-ray spectroscopy and absorbance measurement. Fundamental principle is that the measured signal is change in polarization as the incident radiation which we modified specific incident angle interacts with the thin film structure and substrate for reflected. In addition, from comparing the measured and calculated polarization changes is extracted to the phase difference (Δ), and amplitude ratio (ψ) which can be determined the complex dielectric constant (ϵ). To confirm the optical properties of the thin film layer, we can subtract the substrate information from result.

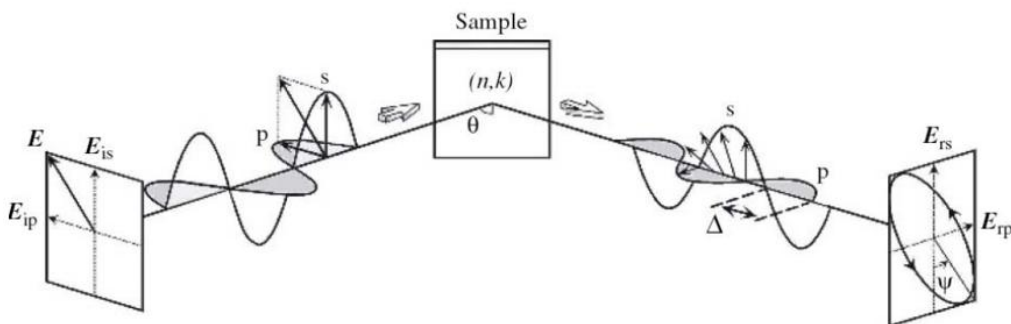


Figure 6. Schematic physics of ellipsometry.

2. Experimental equipment and methodologies

3.1 Thin film growth and structure characterization

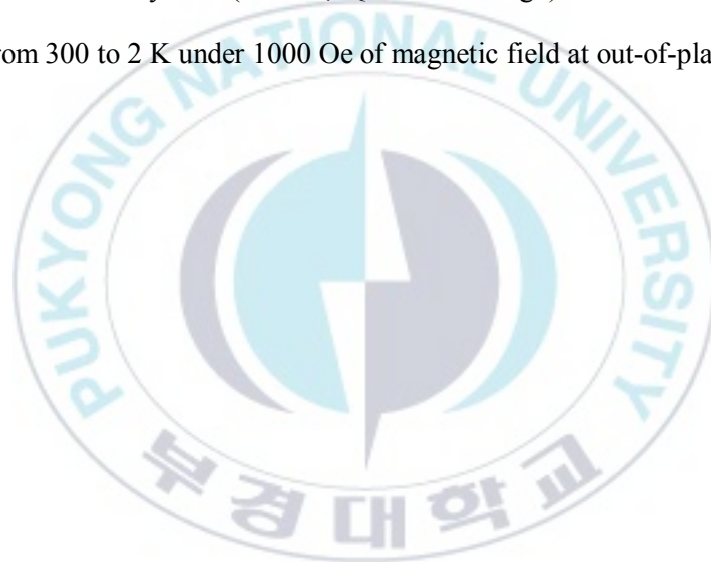
High-quality epitaxial superlattices consisting of alternating SRO/CRO layers were grown on atomically flat SrTiO₃ (001) substrates using pulsed laser deposition (PLD). KrF excimer laser ($\lambda = 248$ nm; Coherent Inc., COMPex 205F) with the fluence of 1.2 J/cm² and a repetition rate of 5 Hz were used for ablation. Substrate temperature was fixed at 750 °C with $P(O_2)$ under 10⁻¹ Torr. The epitaxial relation, crystal orientations, and atomic structure of SLs were characterized using gonio-, φ -, in-plane-scan, and reciprocal space map (RSM) by high resolution and high-power X-ray diffractometer (XRD, Rigaku SmartLab II).

3.2 Electronic structure characterization

The optical conductivity of the CRO, SRO, and SLs thin films were analyzed by spectroscopic ellipsometer (VASE and M-2000, J.A. Woolam Co.). And the optical conductivities measurement conditions were first measured from 1.2 to 6.5 eV, the incident angle was fixed at 75 °, and at room temperature.

3.3 Magnetic moment and resistivity measurements

The *dc*-transport measurement using van der Pauw method studied for the resistivity as a function of temperature, $\rho(T)$, The measurements were conducted electrodes with Au wires, and were processed from 300 to 10 K. The saturation magnetization (M_s) and coercivity field (H_c) from hysteresis loop in SLs was measured using Magnetic property measurement system (MPMS, Quantum Design). The measurements were processed from 300 to 2 K under 1000 Oe of magnetic field at out-of-plane direction.



4. Result & discussion

4.1 Structural characterizations of Superlattices

The high-quality superlattices with a coherent interface can exhibit various physical properties depending on the number of unit cells (UCs) of the layered material. To clearly observe the changes in physical properties, we fixed the SrRuO₃ (SRO) UCs of superlattices (SLs) and changed the number (m) of UCs of the CaRuO₃ (CRO) layer. Figure 7a shows the schematic stacking order of SRO/CRO SLs grown on (0 0 1) - oriented SrTiO₃ (STO) substrates. The stacking period of all superlattices was fixed at 10 with 6 UCs of SRO and inserted m UCs of CRO layer. The SRO/CRO SLs structures with interface-coupling with CRO- and SRO-layers were synthesized using the atomic-scale precision growth of pulsed laser deposition (PLD). To characterize the structure of SLs, Figure 7b shows that the θ - 2θ scans using X-ray diffraction (XRD) of the artificially controlled atomic UCs layers of SRO and CRO ($[(\text{SRO})_n(\text{CRO})_m]_{10} = [n|m]$, $n = 6$ UCs of the SRO and m UCs of the CRO) SLs series on a single-crystalline STO (001) substrate. We observe the well-defined Bragg pronounced thickness fringes, so-called Kiessig and Pendellösung fringes (Figure 8b). This result is a good agreement with the expected values based on the X-ray reflectivity (Figure 9a). Also, all samples show distinct order SLs peaks, indicating a highly repetitive layered structure with a sharp and clear interface. So, from the θ - 2θ scans with [001] direction, we found that the SLs satellites peaks are located nearby the Bragg peaks of superlattices. This result indicates that the SRO/CRO SLs have heterostructures with periodicity. In addition,

Figure 7c shows two representative possibilities of octahedral rotations in the pseudocubic structured perovskite materials. Structurally, the epitaxial thin films have a tensile or a compressive strain due to lattice mismatch between a thin film and substrate. The epitaxial SRO and CRO thin films on STO substrates have different strains, such as compressive and tensile strains, respectively. In the epitaxial thin films, pseudocubic SRO and CRO thin film are represented by an orthorhombic structure with $a^-b^+c^-$ and a tetragonal structure with $a^-a^-c^0$ rotation patterns, Glazer notation system, respectively [23, 24]. To characterize this structural change, reciprocal space mapping (RSM) was studied about the (1 0 3) and (0 1 3) asymmetry reflection of the SLs and STO. Figure 7d reveals that SLs and STO peaks locate the same Q_x values that confirm the films are coherently strained. In addition, SLs have the different Q_z values that were induced by orthorhombic symmetry for specific condition ($m < 2$). And Figure 9 shows that the (2 0 4) asymmetry plane reflections with other symmetry planes also indicate that the different peak positions for SLs ($m = 1$) and SRO thin film which were revealed the orthorhombic structure. Therefore the SLs structure can be easily changed by a little CRO UCs and other studies also show that SRO structure can be easily changed using by STO UCs [22]. In this paper, we show that the crystal symmetry of SLs was changed by stacking of artificial SLs. This result leads that octahedral rotation further could be manipulated by interface-coupling with CRO and SRO layers.[25]

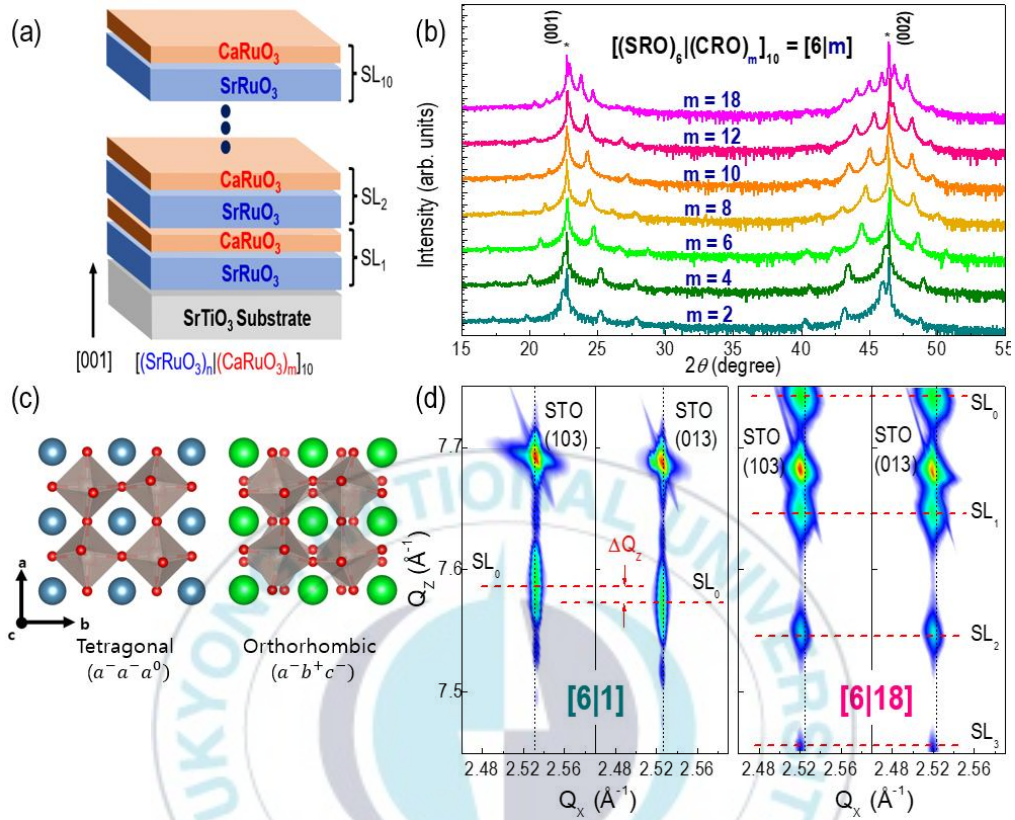


Figure 7. Structural characterizations of $[(\text{SrRuO}_3)_6/(\text{CaRuO}_3)_m]_{10}$ superlattices grown on SrTiO_3 (0 0 1) substrates. (a) Schematic illustration of the stacking order of $\text{SrRuO}_3/\text{CaRuO}_3$ superlattice structures. (b) X-ray scans for all the superlattices with different m unit cells of the CaRuO_3 layer ($[(\text{SrRuO}_3)_6/(\text{CaRuO}_3)_m]_{10} = [6/m]$) around the (0 0 l) Bragg reflections of the SrTiO_3 substrates (*). (c) The pseudocubic unit cell of orthorhombic and tetragonal structure corresponding to the Glazer notation. (d) XRD reciprocal space mappings were measured about the (103) and (013) plane reflection of pseudocubic reflections for $[61]_{10}$ (left) and $[618]_{18}$ (right).

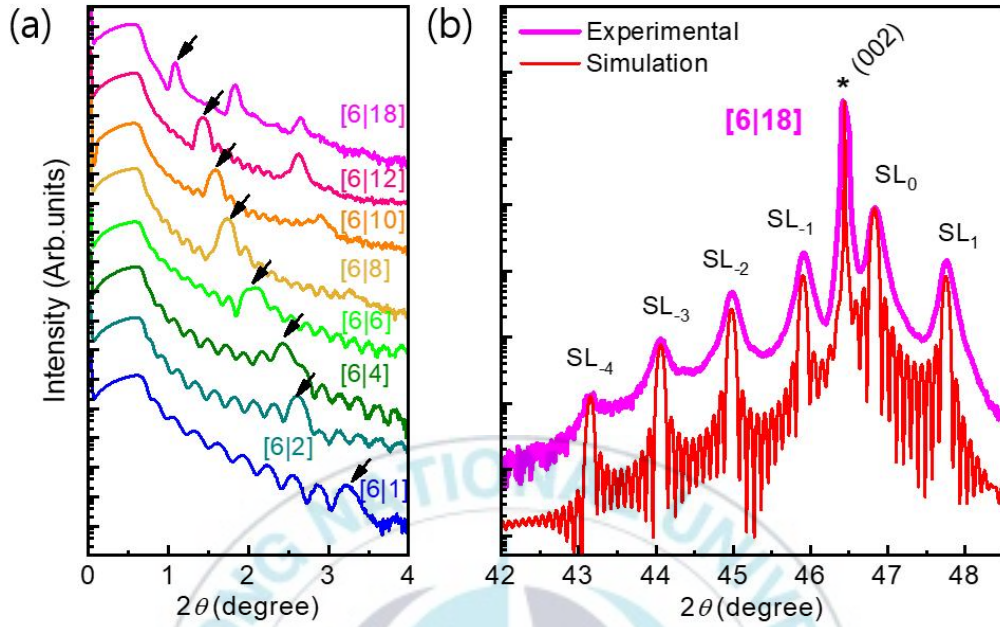


Figure 8. Quantitative structural analysis of $[(\text{SrRuO}_3)_6/(\text{CaRuO}_3)_m]_{10}$ superlattices grown on SrTiO_3 (0 0 1) substrates. (a) X-ray reflectivity measurement for all superlattices with different m unit cells of the CaRuO_3 layer $[6|m]$. Fringes indicated by arrows mean satellite peaks of superlattices. (b) Comparison for the $m = 18$ superlattice with model calculation. The calculation assumes a $[6|18]$ superlattice grown on SrTiO_3 (0 0 1) substrate with lattices distortion.

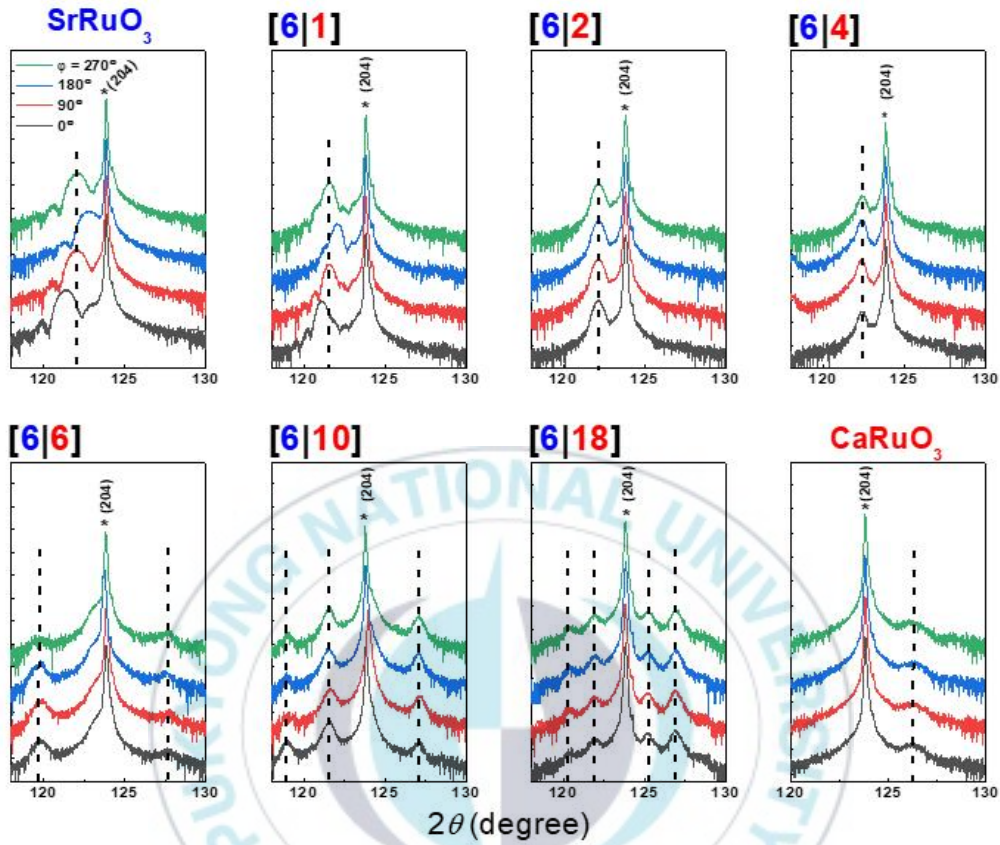


Figure 9. X-ray diffraction (2 0 4) reflections for the rotations of φ -angles of 0, 90, 180, and 270° about $(\text{SrRuO}_3)_6/(\text{CaRuO}_3)_m$ superlattices demonstrated by $[6|m]$. For all the superlattices, peak positions nearly located by SrTiO_3 (204) reflection

4.2 Electronic and magnetic properties

On the basis of the aforementioned, in order to confirm the correlation between the electronic and magnetic properties and the RuO₆ octahedral rotations, we measured whether these physical properties could be changed in artificial SLs. Firstly, *dc*-transport measurements were conducted from 10 to 300 K using van der Pauw geometry [26]. Figure 10a shows that the temperature-dependent resistivity divided by resistivity value measured at a specific temperature (300 K). This result reveals that SRO epitaxial thin film has relatively low resistivity ($50 \sim 200 \mu\Omega \cdot cm$) and the relatively large residual resistivity ratio (*RRR*) (4-6) and long range of ferromagnetism (~ 150 K). While the CRO thin film indicated high resistivity ($10^{-4} - 10^{-3} \Omega \cdot cm$) and relatively low *RRR* (1-2) and no ferromagnetism. In addition, SLs further indicated that *RRR* (defined as $\rho(30 K)/\rho(300 K)$) was sharply decreased by CRO UCs and finally converge to ~ 0.5 and T_C decreased to ~ 90 K at CRO 6 UCs. In general, it has been suggested that the SLs where two different octahedral rotation periodically interact at an interface can significantly affect the octahedral rotation and crystal symmetry of SLs (i.e., Ru-O-Ru bonding angles, Ru-O bond lengths). This result also leads that the Ru *4d* orbitals and the O *2p* orbitals consist with different hybridizations, and these changes indicate the changes the overall electrical transport[4, 5, 27]. Figure 10b show that we studied the temperature-dependent magnetization ($M(T)$) after field-cooled on the out-of-plane direction, which were nearly in the vicinity to the magnetic easy-axis of typical SRO thin films. These result argue that magnetic exchange interactions were occurred between the Ru *d-d* transitions by the changed octahedral rotation of SRO

layers in the SLs. In addition, we studied the Magnetic-field dependent magnetization ($M(H)$) for the SLs. Figure 11 reveals that the SRO films have a relatively high saturated magnetization (M_S) of $\sim 2.30 \mu_B/Ru$ ($\sim 335 \text{ emu/cm}^3$). From the $M(H)$ curves, the M_S of SLs were decreased with an increase in m . while the coercivity field were increased ($m < 8$). From the result, a both of sharply changed resistivity and magnetic moment were distinguished by the specific temperature in the SRO and SLs thin films, and the T_C was determined from the derivative of $R-T$ and $M-T$ and coherently results to be $\sim 148 \text{ K}$. While the CRO had no observation of magnetic phase transition. In addition, Figure 10c show that the T_C value of the SLs was decreased by increasing of the CRO unit cell ($m < 8$). while the T_C value was increased under specific conditions ($m > 6$). These results also indicated that octahedral rotation of SRO changed by interface-interaction with CRO layer in SLs. Furthermore, Figure 10d shows the M_S and H_C for $(\text{SRO})_6/(\text{CRO})_m$ superlattices. H_C was measured by Hysteresis loops at 5 K (Figure 11). From the data, the H_C value of the SLs was increased by increasing of the CRO UCs ($m < 8$). And after 8 UCs, we observed that the magnetization sharply increase at nearby the zero H -field, which is generally originated by the Barkhausen jump with domain effect [28]. This result further leads that SRO and CRO layers had been reconstructed by altering the CRO unit cell. In addition, As increasing the CRO unit cell, the crystal symmetry of SLs changed orthorhombic to tetragonal. As a result, crystal symmetry is going to lower the ground-state magnetic moment. Since The magnetization and orthorhombicity are strongly coupled [29] The M_S of SLs were decreased by increasing the CRO unit cell.

And these similar results were reported from other papers. For example, $\text{Ca}_x\text{Ru}_{1-x}\text{O}_3$

shows that M_s and T_c are decreased by increasing the Ca ratio and finally ferromagnetic ordering disappears by $x = 0.75$ [14]. On the contrary, we found out that the ferromagnetic ordering did not disappear regardless of CRO UCs and can control the T_c of SLs using CRO UCs Over the 6 UCs of CRO ,and we further found out the Barkhausen jump[30] in SLs which were adjusted by CRO UCs and these phenomenon was not founded at $\text{Sr}_{1-x}\text{Ca}_x\text{RuO}_3$ structure [6].

In this paper, the growth of SLs, we have controlled the same state of stoichiometry [31], crystallinity, lattice parameter, and epitaxial strain [32]. As the CRO unit cell increases, M_s of SLs were decreased. Since the structure of SLs was changed from orthorhombic to tetragonal, and SLs has higher crystal symmetry, which is evidence that octahedral rotation of SLs also changed. In addition, T_c also decreased to 65 K and increased large film resistivity in the overall.

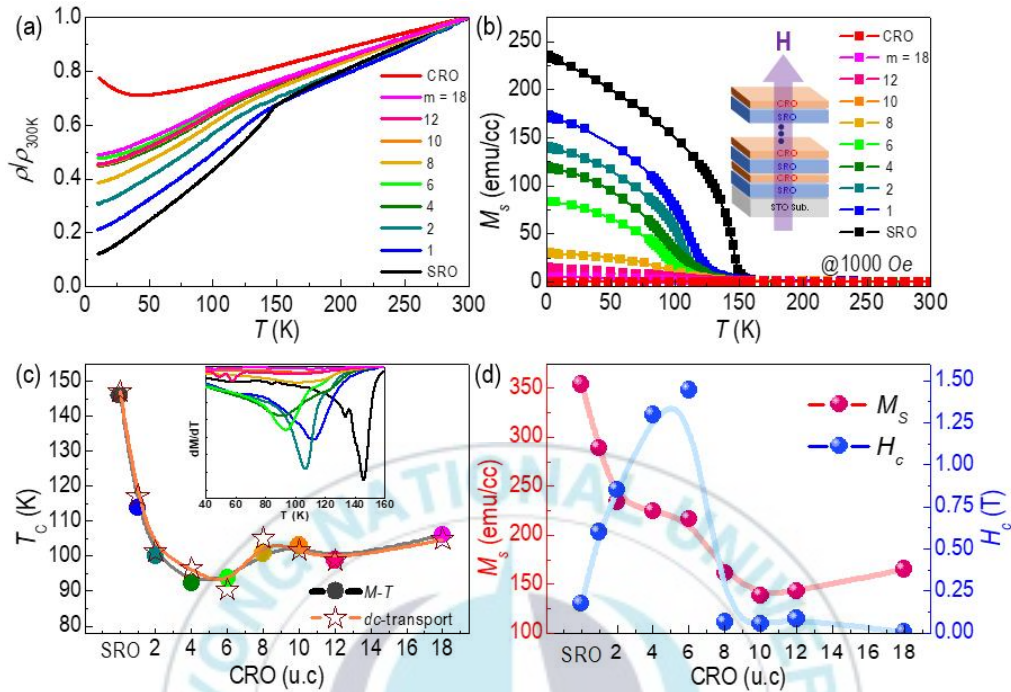


Figure 10. The electronic and magnetic properties of the $(\text{SrRuO}_3)_6/(\text{CaRuO}_3)_m$ superlattices tuned by the CaRuO_3 unit cell. (a) Temperature-dependent electrical resistivity behavior for $(\text{SrRuO}_3)_6/(\text{CaRuO}_3)_m$ superlattices. (b) The magnetic moment as function of temperature was measured after field cooling and under 1,000 Oe of magnetic field along the out-of-plane direction. (c) Ferromagnetic transition temperature (T_c) of SRO and SLs thin film are extracted from $M(T)$ and $R(T)$. (d) coercivity field (H_c) and saturation magnetization for $(\text{SrRuO}_3)_6/(\text{CaRuO}_3)_m$ superlattices

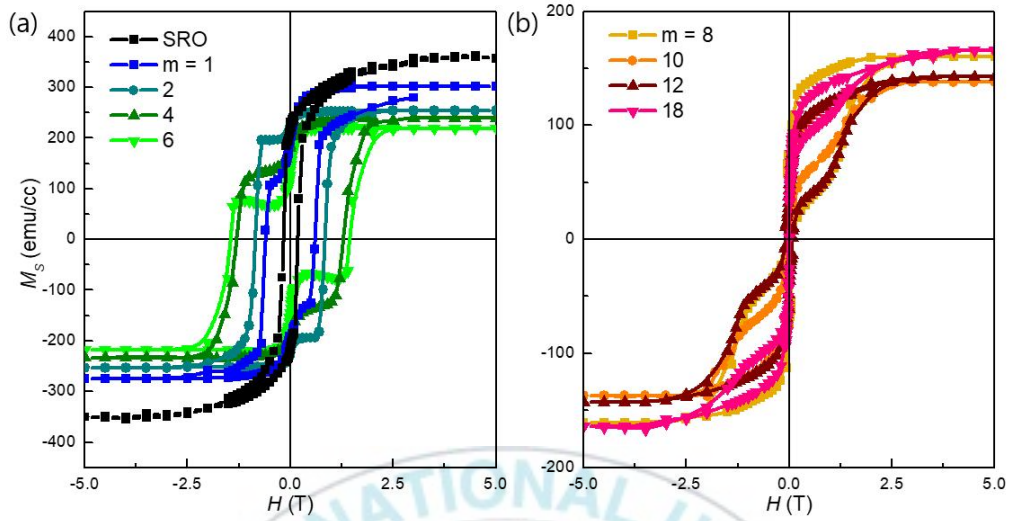


Figure 11. Magnetization (M) versus field (H) of $(\text{SrRuO}_3)_6/(\text{CaRuO}_3)_m$ superlattices at $T = 5$ K for, $m < 8$ unit cells (a) and $m > 6$ unit cells (b)

4.3 Electronic structure of superlattice

To characterize the electronic structure, Figure 12 shows that the optical conductivity results measured by spectroscopic ellipsometry, which indicates the electronic structure of SLs near by the Fermi level. The real part of the optical conductivity spectra, $\sigma_1(\omega)$ (Figure 12a) show that optical transitions of SLs were clearly exhibited by change CRO unit cell. For the detail, three different peaks, labelled as A , β , and B at ~ 3.3 , ~ 4.1 , and ~ 6.2 eV, are attributed to $O\ 2p \rightarrow Ru\ 4d\ t_{2g}$, $Ru\ 4d\ t_{2g} \rightarrow e_g$, and $O\ 2p \rightarrow Ru\ 4d\ e_g$ optical transitions, respectively [33]. In addition, the quantitative hybridization strength between the Ru and O states are directly indicated the optical transition peaks A and B and Ru $4d$ orbital changes related to the optical transition peak β . In order to characterize each individual optical transition which contain the individual information of hybridization. we fitted the optical conductivities using the following Drude-Lorentz equation:

$$\sigma_1(\omega) = \frac{e^2}{m^*} \frac{n_D \gamma_D}{\omega^2 + \gamma_D^2} + \frac{e^2}{m^*} \sum_j \frac{n_j \gamma_j \omega^2}{(\omega_j^2 - \omega^2)^2 + \gamma_j^2 \omega^2} \quad (1)$$

Where e is the electronic charges, m^* is the effective mass of electrons, n is the carrier density of electrons, γ is scattering rate, and ω is resonant frequency. Each subscript of j -th and D indicates the Lorentz and Drude behaviors. From the result, we do not observe the significant changes of the position (ω_j) and the width (γ_j) of the optical transition peaks. But the area of optical transition peak which was described by spectra weight ($W_s \equiv \int \sigma_j(\omega) d\omega \propto n_j / \omega_j$) is observed with changing the CRO

UCs, as shown Figure 12b With increasing CRO UCs, $W_{s\beta}$ and W_{sA} show a systemically increase and decrease.

In the results, we focused on spectra weight of A and β . First optical transition peak A is steadily decreased as the crystal structure of SLs change orthorhombic to tetragonal structure. This denotes that the change in hybridization strength between the Ru and O, due to the charge transfer transitions related an occupied O $2p$ state. Furthermore, the $W_{s\beta}$ could indicate the Ru-O-Ru bond angle. As the crystal structure of SLs change orthorhombic to tetragonal by increasing CRO unit cell, we observed that the $W_{s\beta}$ value increased. This result also leads that the Ru-O-Ru bond angles in SLs increases, and enhances the inter-site $d-d$ transitions due to the much overlap of Ru $4d$ orbitals.

As shown in Figure 12b, it was confirmed that as CRO UCs increased, β increased and, conversely, A pick decreased. At CRO 6 UCs, the spectral weight values of A and β were reversed, and as CRO continued to increase after that, as a result, they moved back to CRO characteristics. According to the above results, as the CRO UCs increases, there is a change in the overall octahedral distortion of the SLs. Also, as the CRO UCs increases, the octahedral distortion in the SLs is decreasing through the transition from the orthorhombic to the tetragonal structure through structural analysis. Our results are consistent with others[4, 5, 33]. To verify the detailed octahedral distortion, direct measurements were carried out and discussed in the section of 4.4.

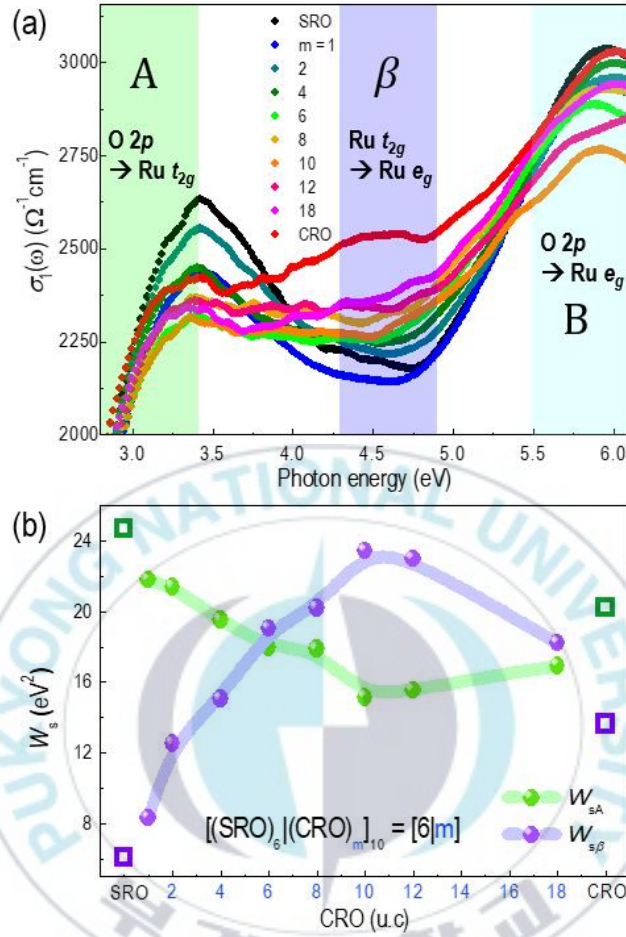


Figure 12. Spectroscopic ellipsometry spectra of the $(\text{SrRuO}_3)_6/(\text{CaRuO}_3)_m$ superlattices. (a) Real part of the optical conductivity, $\sigma_1(\omega)$, of the $(\text{SrRuO}_3)_6/(\text{CaRuO}_3)_m$ superlattices. The optical transitions at ~ 3.2 , ~ 4.4 , and ~ 6.0 eV is assigned as A , β , and B , respectively. (b) Spectral weight (W_s) evolution of the Lorentz oscillators as a function of CaRuO₃ unit cell.

4.4 Half-Order-Peak and RuO₆ octahedral distortion

In bulk, SRO and CRO have the same space group (*Pbnm*) due to consist with same octahedral rotation pattern ($a^- b^- c^+$). but the difference in strain effect on STO substrate, and we observed that CRO and SRO had tensile and comprehensive stress on the STO substrate, respectively. Thus, the octahedral structures in SRO thin film will have an elongation along the [001] direction (Conversely, the *c*-axis of CRO is reduced), Due to the biaxial strain exerted on the STO. The octahedral rotations of CRO and SRO are expected to decrease, and increase compared to the existing bulk. And we suggest that the octahedral rotation at the CRO/SRO interface could be manipulated by interface-coupling between two consecutive layers with different octahedral rotation.

In order to determine the octahedral rotation patterns, we studied the detailed structural analysis using High-power XRD based half-order Bragg peak analysis. And Octahedral rotation information was determined by based on simple analysis rules in perovskite systems. Firstly, to determine the octahedral rotation types, we measured the “odd-odd-odd” and “even-odd-odd” half-order reflections which indicate the out-of-phase octahedral rotations (−) and in-phase octahedral rotations (+), respectively. In addition, *A*-site cation displacement will give rise to “even-even-odd” half-order reflections. From the “odd-odd-odd” half-order reflection measurement each $k \neq l$, $h \neq l$ and $h \neq k$ conditions are an indication of an a^- , b^- , and c^- type rotations, respectively. In addition, the “even-odd-odd” half-order reflection measurement each $k \neq l$, $h \neq l$ and $h \neq k$ conditions are an indication of an a^+ , b^+ , and c^+ type rotations, respectively.

As a result, from the intensity and peak position of specific half-order Bragg peaks, we can quantitatively determine the octahedral rotation and pseudocubic c lattice parameters of SLs by comparing the measured and simulated results. Furthermore, when the orthorhombic structure growth on (0 0 1)-oriented cubic structure, the orthorhombic c -axis will tend to aligned with the step edges of substrate due to the miscut of the STO substrate. Thus, it is possible to have four different structure domains[34]. And when we studied to process fittings for intensities of the half-order Bragg peaks, we have no constraint condition about each volumetric ratio of the four structural domains from the fitting result. To analyze the angle and type for octahedral rotation about each axes based on the rules noted earlier, first, figure 13a shows that three representative peaks for out-of-phase rotation ($-$) information of each axes, which we observed $1/2\ 1/2\ 3/2$, $1/2\ 3/2\ 1/2$, and $1/2\ 3/2\ 3/2$ diffractions. From these results, all out-of-phase rotations ($-$) were measured for each axis, thus we confirm that two out-of-phase rotation ($-$) axes are laid either in-plane or out-of-plane. And figure 13b shows that two $1\ 1/2\ 3/2$ and $1/2\ 1\ 3/2$ diffractions are appearance in SRO and SLs which indicate that the in-phase rotation ($+$) while CRO have no appearance about $1\ 1/2\ 3/2$ and $1/2\ 1\ 3/2$ diffraction peak. This result leads that in-phase rotation ($+$) of SRO and SLs belong to $[100]$ or $[010]$ direction of the STO substrate while CRO have no observed in-phase rotation ($+$). In addition, we can further determine that the decrease of the volumetric symmetry of the four structures from the different peak intensity of $1\ 1/2\ 3/2$ - and $1/2\ 1\ 3/2$ -diffraction peaks. From the result, we figure out that the octahedral rotation patterns of both SRO and SLs have monoclinic structure with $a^+ b^- c^-$ or $a^- b^+ c^-$. While the octahedral rotation pattern of CRO is $a^0 b^- c^-$. In addition, by the increasing CRO unit cell in SLs, we reveal that the $1\ 1/2\ 3/2$ and $1/2\ 1$

$3/2$ diffraction peaks are going to nearly equivalent peak intensities. And it suggests that the volumetric symmetry of domain structure of SLs ($m > 1$) is highly increased by altering CRO unit cell. Furthermore, this result leads that the SLs ($m > 1$) have tetragonal structure which due to volumetric symmetry of domain structure, meanwhile have same monoclinic domain structure like SRO. This result indicates that the symmetry of the octahedral rotation with different domain structures induced decoupling effect for the overall lattice. In addition, Figure 13c shows that peak intensities for the $1/2\ 1\ 2$ and $1\ 1/2\ 2$ diffraction peaks indicating that A-site cation displacement in SLs. These results indicate that in-phase rotation (+) and A-site cation displacement are strongly related and decreased by increasing of CRO UCs. For determining the pseudocubic c lattice parameter of the SLs. First, we assumed the distorted tetragonal (DT) structures with out-of-phase rotations (-). In addition, SRO layers in SLs and SrRuO₃ film only correspond a distorted orthorhombic (DO) phase, which emerges with in-phase rotation (+) along the in-plane axes. Figure 13d shows that the pseudocubic lattice parameter of c -axis (c_p) of the DT and DO phases are determined from the half-order Bragg peaks. First The c_p values of DT which were obtained from the three-half-integer peaks are related both CRO and SRO layers in SLs. And c_p values of DT are consistently decrease with m , which indicated that average of c_p are decreased due to the relatively small c value of the CRO layers. While the c_p values derived from one-half-integer peaks have no significant changes under $m \leq 6$. but after $m > 6$, we observed the dramatically decreased and finally consistently decrease with m . In addition, the c_p of DO is strongly corresponding to SRO, so we confirmed that c_p , In-phase rotation (+) and Sr displacement of SRO layers in superlattices are dramatically changed around $m = 6 \sim 8$. And These results indicate

that ferromagnetic properties would be changed around $m = 6 \sim 8$.

To quantitatively analyze the octahedral rotations and structure domain factors in SLs, we compared the half-order Bragg peak intensities of measured and simulated [35, 36, 37, 38]. The peak intensities were derived by the area of peak, which were measured through various half-order Bragg peaks along the h , k and l directions. In turn, we utilize the intensity of each half-order diffraction peak to acquire precise rotation angles and volumetric fractions of structural domains based on prior methods.

$$I = I_0 \frac{1}{\sin \eta} \frac{1}{\sin 2\theta} \left(\sum_{j=1}^4 D_j |F_{hkl}|^2 \right) \quad (2)$$

$$F_{hkl} = f_{O^{2-}} \sum_{n=1}^{24} \exp[2\pi i(hu_n + kv_n + lw_n)] \quad (3)$$

using Equation (2), one can extract both the octahedral structure factor F_{hkl} (given in Equation (3)) and D_j by fitting the diffraction intensity, where I_0 is the incident light intensity. $\frac{1}{\sin \eta}$ is a correction for the beam footprint, $f_{O^{2-}}$ is the X-ray form factor for O^{2-} [39], and $\frac{1}{\sin 2\theta}$ is the Lorentz polarization correction factor. Python based program was used to determine the optimal fitting parameters including octahedral rotation angles α , β , γ and four structure domain factors by minimizing the sum of the square of the difference between the measured and calculated intensities of certain half-order diffraction peaks.

As noted previously, the octahedral rotation angles and four structure domain factors are quantitatively determined from the comparison of the measured and calculated peak

intensities. Figure 13e shows that the fitted octahedral rotation angles for SRO, CRO, and all SLs films. First, SRO thin film have the rotation angles along the three orthogonal axes are extracted to be $\alpha = 9.1^\circ$ (out-of-plane (-) axis), $\beta = 6.2^\circ$ (in-plane (+) axis), $\gamma = 11.8^\circ$ (out-of-plane (-) axis) whit monoclinic domain structure. While CaRuO₃ thin film have the rotation angles are extracted to be $\alpha = 9.8^\circ$ (out-of-plane (-) axis), $\gamma = 3.4^\circ$ (out-of-plane (-) axis). As noted earlier, we reveal that octahedral rotation decreased or increased under the conditions of comprehensive stress or tensile stress by measuring the half-order-Bragg peaks. Furthermore, we determined that the overall octahedral rotations of SLs are decreased by increasing CRO UCs. Since each CRO- and SRO-layers with different octahedral rotations were interacted at the CRO/SRO interfaces by interface coupling. In addition, to analyze the in-phase rotation (+) which SRO layers only have, it was confirmed that the octahedral rotations of the SRO layer also decreased as the CRO UCs increased, and due to the change of c_p value in SRO layers, the octahedral rotation decrease rapidly around $m = 6 \sim 8$ -unit cell. and in fitting result, four structure domains were calculated by comparative analysis of half-order-Bragg peaks with symmetry planes. As CRO UCs increase, through comparison of peak intensities for $1\ 1/2\ 3/2$ and $1/2\ 1\ 3/2$ diffractions, orthorhombic structure of SRO and SLs ($m = 1$) have low volumetric symmetry due to the different of peak intensities while the tetragonal structure of SLs ($m > 2$) are consist of high volumetric symmetry with the same peak intensity.

In addition, Figure 13f show that Ru-O bond length and Ru-O-Ru bonding angles are calculated using the RuO₆ octahedral rotation angles and the pseudocubic lattice

constant along the c -axis. we calculated two axes of in-plane and out-of-plane. While the CRO UCs increased. For Ru-O-Ru bonding, we observed that the out-of-plane and in-plane bond angle increased up to $m = 10$ and saturated after that. And Out-of-plane and in-plane bond length also changed by changing the CRO unit cell. In SLs, these results lead that the RuO_6 octahedral rotation can be artificially controlled by manipulating SL stacking.



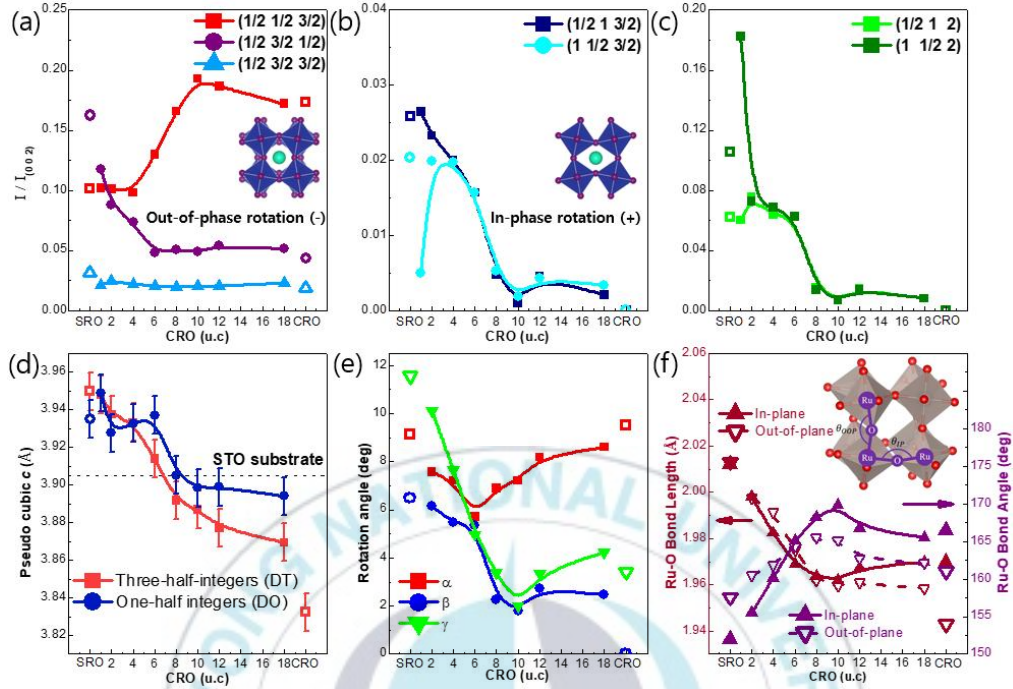


Figure 13. Non-destructive identification for RuO_6 octahedral distortion of $(\text{SrRuO}_3)_6/(\text{CaRuO}_3)_m$ superlattices by HRXRD. Half order Bragg peaks intensity of $(1/2 \ 1/2 \ 3/2)$, $(1/2 \ 3/2 \ 1/2)$ and $(1/2 \ 3/2 \ 1/2)$ (a), $(1/2 \ 1 \ 3/2)$ and $(1 \ 1/2 \ 3/2)$ (b) and $(1/2 \ 1 \ 2)$ and $(1 \ 1/2 \ 2)$ plane (c). Pseudocubic lattice constant along the c axis (c_p) as a function of CRO unit cell determined from half-order Bragg peaks(d). Rotation angles of RuO_6 octahedral (e). Ru-O-Ru bond angles and Ru-O bond length (f) presented as function of CaRuO_3 unit cell. Ru-O-Ru bond angles and Ru-O bond lengths are calculated from RuO_6 octahedral rotation angle and superlattices lattice parameters. The scheme of out-of-phase rotation (-) and in-phase rotation (+) are shown in (a) and (b).

4.5 Correlation between structure and magnetic property

The symmetry of structure was changed orthorhombic to tetragonal and RuO_6 octahedral distortions were reduced by altering superlattices stacking. Figure 14a shows that octahedral distortion and rotation. Comparing the SRO thin film and superlattice ($m = 10$). Total octahedral rotation and A -site displacement largely reduced. From this work, by increasing the CRO unit cell, the octahedral rotation of the overall superlattices were successfully adjusted with the characteristics of the CRO thin film. And due to the orthorhombicity of SLs is decreased, we suggest that orthorhombicity of SRO layers in SLs are also decreased. These results lead that the magnetic properties of SRO and electronic structure of SLs are changed by altering CRO unit cell. First, to confirm electronic structure changes, in the case of the calculated electronic structure which is a large correlation with the in-plane direction component in the ellipsometry described above (Figure 12) lead that the strong correlation between in-plane direction of electronic structure and in-plane Ru-O-Ru bonding angle and length (Figure 14b). This result described that the bonding angle and length between Ru and O which were related with the Ru $d-d$ transitions and $p-d$ hybridization strength were derived by the changes in the octahedral rotation of SLs. Furthermore, In the case of electrical and magnetic properties, we argue that the overall behavior of octahedral rotations were similar to the overall behavior of electrical and magnetic properties. In addition, in the case of the SRO layers in SLs subjected to fully strain, we noted that the in-phase rotation (+) of SLs is strongly related with SRO layers, due to the orthorhombicity of SRO layers. In addition, Figure 14c shows that both the saturation magnetization and

average of the octahedral rotations of SLs were decreased. And it was explained that the octahedral rotations of SRO layers were also decreased through the reduction of the overall octahedral rotations of the SLs. So, we argue that when the octahedral rotations of SRO layers were decreased by SRO/CRO interface interaction, the transition temperature and saturated magnetization were also decreased. Since the magnetic properties of SRO are strongly correlated to Ru-O bond length and Ru-O-Ru bonding angle. To confirm the change of magnetic properties of SLs, we first noted that the SRO layer's lattice parameter was not observed the significant change ($m < 6 \sim 8$). Therefore, there would be no additional effect due to Jahn-Teller distortion and volume effect in SRO layers. This result lead that the Ru-O bond length and Ru-O-Ru bonding angles are purely influenced by octahedral rotation. In addition, in the case of SRO layers subjected to strain on the STO substrate in a previous other study[40], it was confirmed that the transition temperature and saturated magnetization decreased as the octahedral rotation of SRO layers were decreased. In this paper, it is based on SLs subjected to full strain on the substrate, and we also confirmed that the transition temperature and saturation magnetization were adjusted by altering the octahedral rotations of SRO layers using SRO/CRO interface interaction.

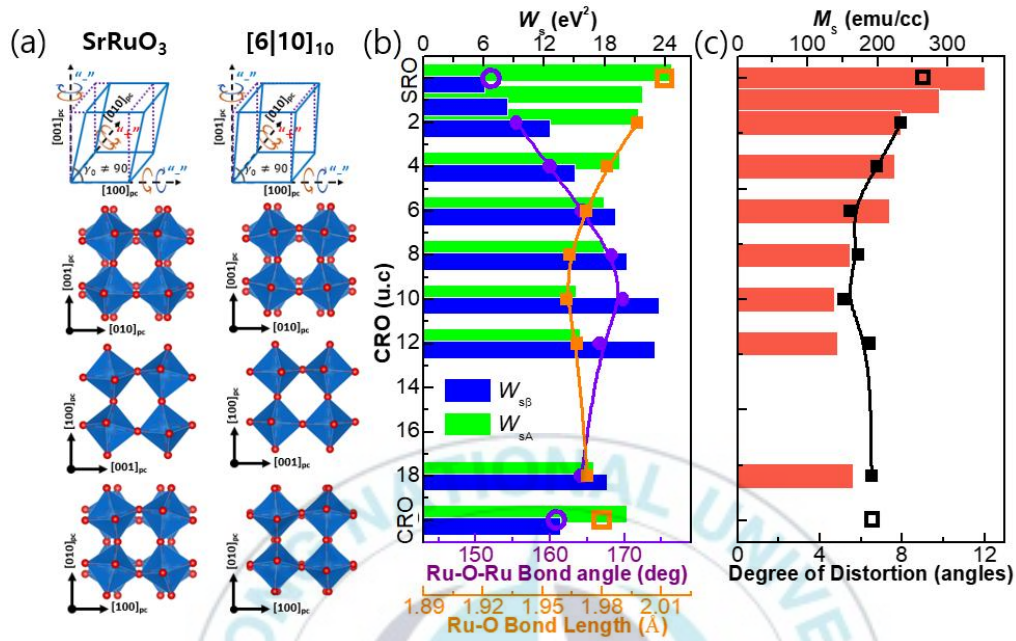


Figure 14. Correlation between RuO₆ octahedral rotation and electronic structure properties of the (SrRuO₃)₆/(CaRuO₃)_m superlattices tuned by the CaRuO₃ unit cell. (b) In-plane Ru-O-Ru bond angles and the transition correspond d-d transition between Ru 4d t_{2g} and e_g states (β) are coherently matched. In-plane Ru-O bond length and charge transfer transition between O 2p and Ru 4d t_{2g} states (A) are coherently matched. (b) coercivity field (H_c) and saturation magnetization for (SrRuO₃)₆/(CaRuO₃)_m superlattices. Saturation magnetization contains only SrRuO₃ layers magnetization properties

5. Conclusion

In conclusion, we have demonstrated that the epitaxially-strained SRO/CRO superlattices with different stacking orders to investigate the role of RuO_6 octahedra attributing physical properties of perovskite ruthenates. It was verified that crystal structure and electrical and magnetic characteristics of perovskite ruthenates can be tuned by manipulating the octahedral rotations in SRO/CRO superlattice.

The octahedral rotations and crystal structure were determined in SRO/CRO SLs with an increasing the CRO UCs. In SLs, with increasing the thickness of CRO sublayers ($1 < m < 18$), the structure of superlattice became tetragonal from orthorhombic due to the suppression of the degree of overall octahedral rotations.

The detailed structural investigations by the systematical analyses of the multiple half-order Bragg peaks for the superlattices have revealed that the type of octahedral rotation is $a^+ b^- c^-$ for all superlattices. The observed octahedral rotation of $a^+ b^- c^-$ was diminished and the volume fraction of the different rotational domains were going to be more equivalent by increasing m (the number of CRO UCs), which results in the structural conversion of superlattices from orthorhombic to tetragonal phase.

It is also noting that the electronic structure is strongly modulated with the changes in Ru-O-Ru bond angles and lengths of RuO_6 octahedron.

The control of octahedral configuration by designing superlattice structure including layer stacking and composition provides a novel framework for harnessing electronic and magnetic properties of multifunctional perovskite oxides. Furthermore, these

findings provide us novel possibilities that the electronic structure affecting physical properties can be tuned by octahedral engineering for future oxide electronic and spintronic applications.



References

- [1] Lu, W., W. Song, P. Yang, J. Ding, G.M. Chow and J. Chen, Strain Engineering of Octahedral Rotations and Physical Properties of SrRuO_3 Films. *Scientific Reports*. 5 (2015) 10245.
- [2] Masys, Š. and V. Jonauskas, A First-Principles Study of Structural and Elastic Properties of Bulk SrRuO_3 . *The Journal of Chemical Physics*. 139 (2013) 224705.
- [3] Herklotz, A. and K. Dörr, Characterization of Tetragonal Phases of SrRuO_3 under Epitaxial Strain by Density Functional Theory. *The European Physical Journal B*. 88 (2015) 60.
- [4] Lee, S.A., et al., Correlation between Ru–O Hybridization and the Oxygen Evolution Reaction in Ruthenate Epitaxial Thin Films. *Sustainable Energy & Fuels*. 3 (2019) 2867-2872.
- [5] Lee, S.A., et al., Tuning Electromagnetic Properties of SrRuO_3 Epitaxial Thin Films Via Atomic Control of Cation Vacancies. *Scientific Reports*. 7 (2017) 11583.
- [6] Nguyen, L.T., M. Abeykoon, J. Tao, S. Lapidus and R.J. Cava, Long-Range and Local Crystal Structures of the $\text{Sr}_{1-x}\text{Ca}_x\text{RuO}_3$ Perovskites. *Physical Review Materials*. 4 (2020) 034407.
- [7] Akamatsu, H., K. Fujita, T. Kuge, A.S. Gupta, J.M. Rondinelli, I. Tanaka, K. Tanaka and V. Gopalan, *A*-Site Cation Size Effect on Oxygen Octahedral Rotations in Acentric Ruddlesden-Popper Alkali Rare-Earth Titanates. *Physical Review Materials*. 3 (2019) 065001.
- [8] Parul Pandey, C.-H.C., Angus Huang, Rakesh Rana, Changan Wang, Chi Xu, Horng-Tay Jeng, Manfred Helm, R. Ganesh, Shengqiang Zhou, Carrier Driven Antiferromagnetism and Exchange-Bias in $\text{SrRuO}_3/\text{CaRuO}_3$ Heterostructures. arXiv:1802.05869. (2018).
- [9] Cheng, J.G., J.S. Zhou and B. Goodenough John, Lattice Effects on Ferromagnetism in Perovskite Ruthenates. *Proceedings of the National Academy of Sciences*. 110 (2013) 13312-13315.
- [10] Dang, H.T., J. Mravlje, A. Georges and A.J. Millis, Electronic Correlations, Magnetism, and Hund's Rule Coupling in the Ruthenium Perovskites SrRuO_3 and CaRuO_3 . *Physical Review B*. 91 (2015) 195149.
- [11] Felner, I. and U. Asaf, Magnetic Studies of $\text{Ca}_{1-x}\text{M}_x\text{RuO}_3$ (M=La and Sr). *Physica B: Condensed*

- Matter. 337 (2003) 310-317.
- [12] Longo, J.M., P.M. Raccach and J.B. Goodenough, Magnetic Properties of SrRuO_3 and CaRuO_3 . *Journal of Applied Physics*. 39 (1968) 1327-1328.
- [13] Yoshimura, K., T. Imai, T. Kiyama, K.R. Thurber, A.W. Hunt and K. Kosuge, ^{17}O Nmr Observation of Universal Behavior of Ferromagnetic Spin Fluctuations in the Itinerant Magnetic System $\text{Sr}_{1-x}\text{Ca}_x\text{RuO}_3$. *Physical Review Letters*. 83 (1999) 4397-4400.
- [14] Mazin, I.I. and D.J. Singh, Electronic Structure and Magnetism in Ru-Based Perovskites. *Physical Review B*. 56 (1997) 2556-2571.
- [15] Lytle, F.W., X Ray Diffractometry of Low Temperature Phase Transformations in Strontium Titanate. *Journal of Applied Physics*. 35 (1964) 2212-2215.
- [16] Chan, N.H., R.K. Sharma and D.M. Smyth, Nonstoichiometry in SrTiO_3 . *Journal of The Electrochemical Society*. 128 (1981) 1762-1769.
- [17] Pai, Y.-Y., A. Tylan-Tyler, P. Irvin and J. Levy, Physics of SrTiO_3 -Based Heterostructures and Nanostructures: A Review. *Reports on Progress in Physics*. 81 (2018) 036503.
- [18] Benthem, K.v., C. Elsässer and R.H. French, Bulk Electronic Structure of SrTiO_3 : Experiment and Theory. *Journal of Applied Physics*. 90 (2001) 6156-6164.
- [19] Vailionis, A., W. Siemons and G. Koster, Room Temperature Epitaxial Stabilization of a Tetragonal Phase in ArRuO_3 ($a=\text{Ca}$ and Sr) Thin Films. *Applied Physics Letters*. 93 (2008) 051909.
- [20] Gunasekera, J., L. Harriger, T. Heitmann, A. Dahal, H. Knoll and D.K. Singh, Quasilocal Critical Nature of Cooperative Paramagnetic Fluctuations in CaRuO_3 Metal. *Physical Review B*. 91 (2015) 241103.
- [21] Tripathi, S., R. Rana, S. Kumar, P. Pandey, R.S. Singh and D.S. Rana, Ferromagnetic CaRuO_3 . *Scientific Reports*. 4 (2014) 3877.
- [22] Jeong, S.G., et al., Propagation Control of Octahedral Tilt in SrRuO_3 Via Artificial Heterostructuring. *Advanced Science*. 7 (2020) 2001643.

- [23] Vailionis, A., H. Boschker, W. Siemons, E.P. Houwman, D.H.A. Blank, G. Rijnders and G. Koster, Misfit Strain Accommodation in Epitaxial Abo_3 Perovskites: Lattice Rotations and Lattice Modulations. *Physical Review B*. 83 (2011) 064101.
- [24] Glazer, A., The Classification of Tilted Octahedra in Perovskites. *Acta Crystallographica Section B*. 28 (1972) 3384-3392.
- [25] Moon, E.J., R. Colby, Q. Wang, E. Karapetrova, C.M. Schlepütz, M.R. Fitzsimmons and S.J. May, Spatial Control of Functional Properties Via Octahedral Modulations in Complex Oxide Superlattices. *Nature Communications*. 5 (2014) 5710.
- [26] Van Der Pauw L, J., A Method of Measuring the Resistivity and Hall Coefficient on Lamellae of Arbitrary Shape. *Philips Technical Review*. 20 (1958) 220-224.
- [27] Jeong, D.W., et al., Temperature Evolution of Itinerant Ferromagnetism in SrRuO_3 Probed by Optical Spectroscopy. *Physical Review Letters*. 110 (2013) 247202.
- [28] He, Q.L., et al., Tailoring Exchange Couplings in Magnetic Topological-Insulator/Antiferromagnet Heterostructures. *Nature Materials*. 16 (2017) 94-100.
- [29] Singh, D.J., Electronic and Magnetic Properties of the 4d Itinerant Ferromagnet SrRuO_3 . *Journal of Applied Physics*. 79 (1996) 4818-4820.
- [30] Kaur, P., K.K. Sharma, R. Pandit, R.J. Choudhary and R. Kumar, Structural, Electrical, and Magnetic Properties of SrRuO_3 Thin Films. *Applied Physics Letters*. 104 (2014) 081608.
- [31] Siemons, W., G. Koster, A. Vailionis, H. Yamamoto, D.H.A. Blank and M.R. Beasley, Dependence of the Electronic Structure of SrRuO_3 and Its Degree of Correlation on Cation Off-Stoichiometry. *Physical Review B*. 76 (2007) 075126.
- [32] Zayak, A.T., X. Huang, J.B. Neaton and K.M. Rabe, Structural, Electronic, and Magnetic Properties of SrRuO_3 under Epitaxial Strain. *Physical Review B*. 74 (2006) 094104.
- [33] Lee, J.S., et al., Optical Investigation of the Electronic Structures of $\text{Y}_2\text{Ru}_2\text{O}_7$, CaRuO_3 , SrRuO_3 , and $\text{Bi}_2\text{Ru}_2\text{O}_7$. *Physical Review B*. 64 (2001) 245107.
- [34] Jiang, J.C., W. Tian, X.Q. Pan, Q. Gan and C.B. Eom, Domain Structure of Epitaxial SrRuO_3

- Thin Films on Miscut (001) SrTiO₃ Substrates. *Applied Physics Letters*. 72 (1998) 2963-2965.
- [35] Jia, C.L., S.B. Mi, M. Faley, U. Poppe, J. Schubert and K. Urban, Oxygen Octahedron Reconstruction in the SrTiO₃/LaAlO₃ Heterointerfaces Investigated Using Aberration-Corrected Ultrahigh-Resolution Transmission Electron Microscopy. *Physical Review B*. 79 (2009) 081405.
- [36] Glazer, A., Simple Ways of Determining Perovskite Structures. *Acta Crystallographica Section A*. 31 (1975) 756-762.
- [37] May, S.J., J.W. Kim, J.M. Rondinelli, E. Karapetrova, N.A. Spaldin, A. Bhattacharya and P.J. Ryan, Quantifying Octahedral Rotations in Strained Perovskite Oxide Films. *Physical Review B*. 82 (2010) 014110.
- [38] Brahlek, M., A.K. Choquette, C.R. Smith, R. Engel-Herbert and S.J. May, Structural Refinement of Pbnm-Type Perovskite Films from Analysis of Half-Order Diffraction Peaks. *Journal of Applied Physics*. 121 (2017) 045303.
- [39] Hovestreydt, E., On the Atomic Scattering Factor for O₂. *Acta Crystallographica Section A*. 39 (1983) 268-269.
- [40] Gao, R., et al., Interfacial Octahedral Rotation Mismatch Control of the Symmetry and Properties of SrRuO₃. *ACS Applied Materials & Interfaces*. 8 (2016) 14871-14878.

Publications

Conferences

K.S. Kim, J. -Y. Hwang, KPS Fall meeting, October 20-22, virtual Conference (2021, Korea)

K. S. Kim, J. -Y. Hwang, Bull. of International Conference on Advanced Materials and Devices, 1095, No. 12 (2021, Korea).

Awards

Best poster presentation award, K.S. Kim, J. -Y. Hwang, KPS Fall meeting, October 20-22, virtual Conference (2021, Korea)

